

Imaging cold atoms with shot-noise and diffraction limited holography

J. P. Sobol* and Saijun Wu†

Department of Physics, College of Science, Swansea University, Swansea, SA2 8PP, United Kingdom

We demonstrate shot-noise and diffraction limited holographic imaging of cold atoms. A ^{87}Rb magneto-optical trap is imaged with a hybrid holographic microscope, where a simple iterative algorithm robustly removes the twin image of the atomic sample during image reconstruction. Shot-noise limited phase shift and absorption images are consistently retrieved at various probe detunings, and during the laser cooling process. Using a camera with a maximum pixel count of $N_{\text{max}} = 2^{14} - 1$, we consistently resolve less than 2 mrad of probe light phase shift by an atomic cloud, outperforming shot-noise limited phase-contrast imaging by a factor of 4 or more.

PACS numbers: 67.85.-d, 42.40.-i, 37.10.Jk, 42.50.-p

Since the achievement of Bose-Einstein condensation [1], many-body physics in textbooks has been reproduced with beautiful experiments in laser cooling labs. Owing to its controllability and precision, the field of ultra-cold atoms holds unique promise for both answering important questions in condensed matter physics, and to generate new physics. Breakthroughs in cold atom research are often accompanied with improved imaging techniques [2]. Recently, in situ imaging [3, 4] has been developed to probe the shortest length scales of the confined, sub- μK quantum gases and is referred to as quantum gas microscopy.

In situ imaging of high density atomic gases suffers from detrimental effects related to resonant interactions mediated by photons. For example, state-of-the-art in situ fluorescence detection [3–5] cannot image an optical lattice site with more than one atom occupancy without losing the extra atoms in pairs. Similarly, absorption imaging is perturbed by resonant dipole interactions, and the atomic density information cannot be faithfully retrieved via the Beer-Lambert law [6]. To mitigate the effect one may saturate the optical transition with a strong probe, which results in images with excessive photon shot noise [7, 8]. Off resonant imaging [9–12] provides a solution to the density dependent line-broadening problem, since the variation of probe light phase shift due to line shape changes vanishes at large detuning. However, the magnitude of the phase shift due to a single atom reduces with detuning, while the phase shift sensitivity is limited by the photon shot noise as $\delta\phi \sim 1/\sqrt{N_p}$, where N_p is the average number of probe photons detected by a pixel. Since $N_p < N_{\text{max}}$, the maximum pixel count, it is difficult with phase-contrast imaging to achieve a sensitivity below 5 mrad using standard cameras, and the amount of detuning allowed for off-resonant detection of cold atoms is correspondingly limited.

The present work demonstrates diffraction limited holographic imaging of cold atoms with photon shot-noise limited sensitivity [13]. Holographic mi-

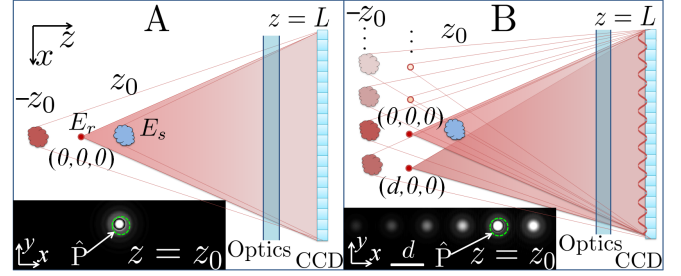


FIG. 1: Schematics of a holographic microscope in the inline (A) and hybrid (B) geometries. A CCD camera records the hologram $H = |E_s + E_r|^2$. A one-step numerical reconstruction of E_s leads to an image at $z = z_0$, and the twin and DC images at $z \approx -z_0$ and $z = 0$ respectively. The insets display slices of the reconstructed $|E_s^{(0)}|$ at $z = z_0$. An aperture \hat{P} is used for iterative removal of the twin and DC images.

croscopy [14] reconstructs a complex wavefront E_s from a hologram H that contains the interference pattern between E_s and a known spherical wavefront E_r (Fig. 1A). Holographic imaging can be free from lens aberrations at large numerical aperture (NA) [15], which is particularly useful for imaging cold atoms at long working distances [2–5]. It is known that an image reconstructed in an inline holographic geometry (Fig. 1A) is contaminated by an out-of-focus twin image [14, 16]. We introduce a hybrid geometry (Fig. 1B) to solve the twin image and DC noise problems. By taking advantage of point source holographic recording, we achieve ~ 2 mrad phase shift and $\sim 0.4\%$ absorption sensitivities, beyond the photon shot noise limit imposed by N_{max} in standard imaging [17]. The sensitivity is near the single atom level with resonant probing. By improving the spatial resolution of $x_{\text{res}} \sim 5.2 \mu\text{m}$ to the wavelength limit, which would not require precision high-NA optics [15], we expect dramatic improvement of the detection sensitivity, allowing off-resonant single atom imaging. With these features, we discuss the method for off-resonant imaging of high density ultra-cold gases, and for non-destructive probing of optical lattices with multiple atom occupancy per site.

Our microscope is depicted in Fig. 1B, together with the traditional inline setup [14] in Fig. 1A. To gener-

*brynsob@yahoo.co.uk

†saijun.wu@swansea.ac.uk

ate the reference wave $E_r = E_{r,1} + E_{r,2}$ in the hybrid setup, we add a second, “off-axis” point source $E_{r,2}$ at $\mathbf{r}_2 = (d, 0, 0)$ displaced from the inline source $E_{r,1}$ at $\mathbf{r}_1 = (0, 0, 0)$ with light power $P_2 = \eta P_1$, resulting in an interference pattern at the camera plane $z = L$. In both setups, the known wavefront E_r interferes with E_s , the elastically scattered light from the sample at $z = z_0$. The light intensity is recorded as the hologram $H = |E_r + E_s|^2$. With H_0 the hologram taken without the sample, an approximation of the 2D wavefront $E_s(L)$ [18] is written as

$$E_H = \frac{H - H_0}{E_r^*} = E_s + \frac{E_r E_s^*}{E_r^*} + \frac{|E_s|^2}{E_r^*}. \quad (1)$$

Using the angular spectrum method [19] we propagate E_H from $z = L$ to $z = z_0$. Specifically, $E(z) = \hat{U}(z - L)E(L)$ where $\hat{U}(z) = \hat{F}^{-1}e^{iz\sqrt{k^2 - k_x^2 - k_y^2}}\hat{F}$, $k = 2\pi/\lambda$ and \hat{F} is the 2D Fourier transform with $E(k_x, k_y, z) = \hat{F}E(x, y, z)$. In addition to E_s focusing at $z = z_0$, the 2nd and 3rd terms in Eq. (1) focus at $z \approx -z_0$ and $z = 0$ as the twin and DC images respectively. Optics between the sample and camera can be modeled for aberration correction. Without aberrations, the resolution of $E_s(z_0)$ is diffraction limited to $x_{\text{res}} = \lambda\sqrt{w^2/4 + (L - z_0)^2}/w$, with w the camera width.

To isolate the real image $E_s(z_0)$, we notice that $E_s(z_0)$ is in focus, while the twin and DC terms are spread out at $z = z_0$ (Fig. 1). With an aperture operator \hat{P} that sets the data outside of the sample area with diameter a to zero, the energy of the out-of-focus images can be removed iteratively with an algorithm similar to ref. [20],

$$\begin{aligned} E_s^{(0)} &= \hat{U}_0 E_H, \\ E_s^{(n+1)} &= \hat{U}_0 \hat{C} \hat{U}_0^{-1} (E_s^{(0)} - \hat{P} E_s^{(n)}). \end{aligned} \quad (2)$$

Here $\hat{U}_0 \equiv \hat{U}(z_0 - L)$, so \hat{U}_0 and \hat{U}_0^{-1} transform the wavefronts between the camera and sample planes. \hat{C} is a conjugation operator $\hat{C}E = E^* E_r / E_r^*$, that converts any wavefront at the camera plane into that of its twin. With $E_s^{(n)} = E_s(z_0) + \delta E_s^{(n)}$ in Eq. (2), the error $\delta E_s^{(n)}$ is easily shown to converge near zero [21] (Fig. 2A). Specifically, the residual energy fraction $r = \int |E_s^{(n)} - E_s(z_0)|^2 dx dy / \int |E_s(z_0)|^2 dx dy$ decays with a characteristic constant $N_0 \approx -1/\log(\epsilon)$,

$$\epsilon = \frac{\int |\hat{P} \hat{U}_0 \hat{C} \hat{U}_0^{-1} \hat{P} I|^2 dx dy}{\int |\hat{U}_0 \hat{C} \hat{U}_0^{-1} \hat{P} I|^2 dx dy}. \quad (3)$$

Here ϵ is the fraction of energy of the out-of-focus twin image $\hat{U}_0 \hat{C} \hat{U}_0^{-1} \hat{P} I$, that is contained within the aperture \hat{P} at z_0 ($I(x, y) = 1$ is a 2D uniform wavefront so $\hat{P} I$ is the image of the aperture itself.). The aperture \hat{P} must be larger than the sample, thus ϵ can characterize the overlap between the real and twin images. To improve the convergence speed one needs to reduce the overlap.

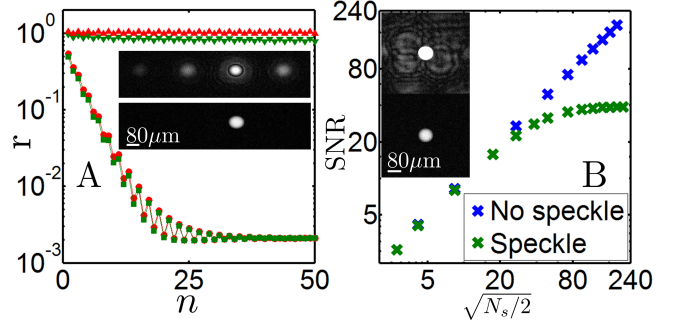


FIG. 2: A) Convergence of the twin image removal algorithm for a simulated phase object. The residual r is plotted vs n for $F = 3.8$ and $F = 28$ with squares and circles respectively in the hybrid geometry ($\eta = 0.16$), and with inverted triangles and triangles respectively in the inline geometry. Inset): The one-step $|E_s^{(0)}|$ (top) and converged $|E_s^{(n=50)}|$ (bottom) for $F = 28$, $\eta = 0.16$. B) Simulated SNR of the converged $|E_s^{(n)}|$ vs $\sqrt{N_s/2}$ in the presence of photon shot noise (blue crosses), and of both speckle and shot noise (green crosses). Inset): the converged $|E_s^{(n=50)}|$ for a strong (top) and a weak (bottom) phase object in the presence of the same speckle noise.

For the inline geometry (Fig. 1A) a large sample needs an aperture with a Fresnel number $F = a^2/2z_0\lambda > 1$, leading to a reduced diffraction effect and thus $\epsilon \approx 1$. In the hybrid geometry the twin image is split into multiple copies displaced by $\mathbf{r}_2 - \mathbf{r}_1$ (Fig. 1B). It is easy to show that the twin image that is inline with the sample takes a fractional energy of $(1 - \eta)^2$ for $\eta < 1$. Thus even for $F \gg 1$, $\epsilon \approx (1 - \eta)^2$ can still be small. In Fig. 2A we plot the residual r vs iteration number for a simulated phase object. For the hybrid scheme with $\eta = 0.16$, the series converges quickly with $N_0 = 2.8 \approx -1/\log(1 - \eta)^2$ for both $F = 3.8, 28$. The non-zero final residual in the simulation is mainly due to the boundary artifacts in the FFT. In contrast, the inline scheme fails to converge within 10^3 iterations even for $F = 3.8$.

So far, we have discussed reconstructing E_s from noiseless holograms with a perfect E_r . Major sources of noise are imperfect subtraction $H - H_0$, aberrations and speckle noise in E_r and E_s , and photon shot noise in H and H_0 . The subtraction is critical for reaching the shot noise limit, for which we developed an optimization algorithm [22]. Photon shot noise in H and H_0 is proportional to $\sqrt{N_p}$ at each pixel with area A_p . Assuming an equal shot noise level in H and H_0 , the root mean square (rms) $E_s^{(n)}$ shot noise level is found to be $\sqrt{2\hbar\omega/A_r Q \tau}$ [22] ($\hbar\omega$, τ , Q and $A_r = x_{\text{res}}^2$ are the photon energy, exposure time, quantum efficiency, and resolution area respectively.). We found the noise penalty to the twin image removal is negligible except when both $a/z_0 \gg \text{NA}$ and $\eta \ll 1$, a regime easily avoided in the hybrid geometry [22]. The signal-to-noise ratio (SNR) of the converged $|E_s^{(n)}|$ is thus shot-noise limited to $\sqrt{N_s/2}$ with $N_s = \langle |E_s(z_0)|^2 \rangle A_r Q \tau / \hbar\omega$ [13]. Remarkably, the

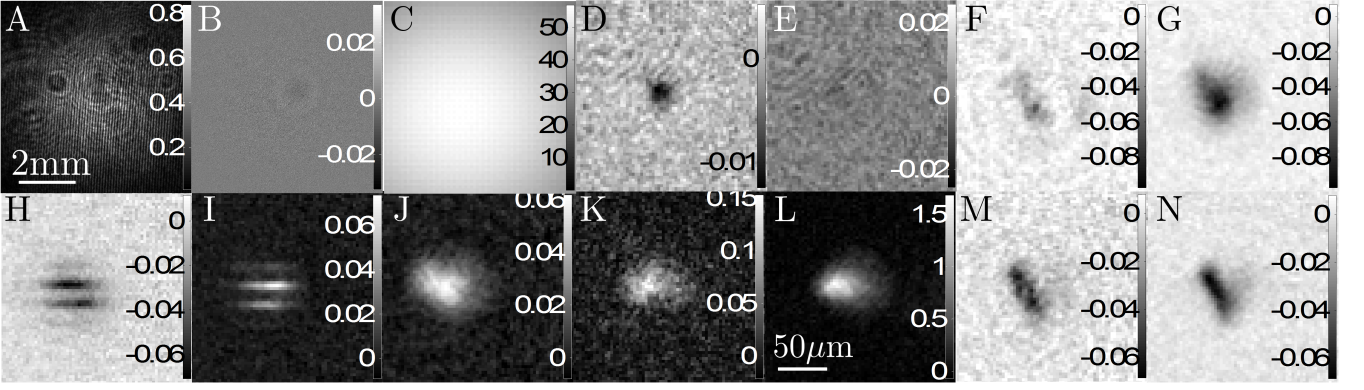


FIG. 3: Holographic reconstructions (D-N), and intensity images (W/m^2) during the reconstruction process (A-C). The hologram H in A) and the subtracted hologram $H - H_0$ in B) obey the 2 mm scale bar. The $|E_{r,1}(z_0)|^2$ in C), and images in D)-N) obey the $50 \mu\text{m}$ scale bar. D) and E) $[\Delta = 30 \Gamma, \tau = 100 \mu\text{s}]$: Phase shift ϕ and absorption coefficient α images reconstructed from B). F) and G) $[\Delta = 1.9 \Gamma, \tau = 100 \mu\text{s}]$: α and ϕ images. H) $[\Delta = 1.9 \Gamma, \tau = 20 \mu\text{s}]$ and I) $[\Delta = -7.1 \Gamma, \tau = 20 \mu\text{s}]$: ϕ images with $20 \mu\text{m}$ fringes. J) $[\Delta = -7.1 \Gamma, \tau = 100 \mu\text{s}]$: ϕ image. K) $[\Delta = 0 \Gamma, \tau = 800 \mu\text{s}]$: atom column density ρ ($1/\mu\text{m}^2$). L) $[\Delta = 0 \Gamma, \tau = 10 \text{ms}]$: ρ image during cooling. M) and N): Same as F) and G) but during cooling.

SNR of the reconstructed image is not sensitive to a change in L , and is only a factor of two less than the $\text{SNR} \rightarrow \sqrt{2N_s}$ [23, 24] in standard absorption or phase-contrast imaging where effectively $L \approx z_0$ within the depth of view. By taking holograms at $L \gg z_0$ to reduce the intensity of the point-source reference fields, the phase shift sensitivity, defined at $\text{SNR}=1$ within A_r , is improved from $\delta\phi = \sqrt{A_p/2A_rN_{\text{max}}}$ in standard imaging to $\delta\phi \approx \sqrt{2\kappa A_p/A_rN_{\text{max}}}$, with $\kappa = |E_r(L)/E_r(z_0)|^2$ [22].

Addressing atomic transitions requires a laser with a long coherence length. Thus holograms of cold atoms can have significant speckle noise (Fig. 3A), which is typically due to distant point-like scatterers. The speckle noise E_{speck} compromises our knowledge of $E_r = E_{r,1} + E_{r,2} + E_{\text{speck}}$. Ignorance of E_{speck} leads to multiple copies of $E_s(z_0)$ shifted by the corresponding distances between the distant scatterers and $\mathbf{r}_{1,2}$, that blur the reconstructed $E_s(z_0)$ image (Fig. 2B). In Fig. 2B we plot the SNR of the converged $|E_s^{(n)}|$ vs $\sqrt{N_s}/2$, simulated in the presence of both speckle and photon shot noise. As expected, the reconstruction can be shot-noise limited if the speckle noise induced blurring of $E_s(z_0)$ is weak.

We demonstrate the hybrid microscope with a simple experiment: A ^{87}Rb magneto-optical trap (MOT) [25] is formed at the center of a vacuum glass cell. The atoms are cooled to $\sim 80 \mu\text{K}$ and holographically imaged by a camera (PCO pixelfly, 1392×1040 pixels, $x_{\text{cam}} = 6.45 \mu\text{m}$ pixel pitch) placed outside the cell. The reference fields $E_{r,1}$ and $E_{r,2}$, detuned by Δ from the D2 hyperfine $F = 2 - F' = 3$ cooling transition ($\lambda = 780.2 \text{ nm}$), are formed by focusing two parallel, linearly polarized laser beams to diffraction limited spots of $3.5 \mu\text{m}$, and $5.2 \mu\text{m}$ respectively. With the focal points $\mathbf{r}_{1,2}$ displaced by $d = 387 \mu\text{m}$, an interference pattern with fringe periodicity $96 \mu\text{m}$ is captured by the camera at $L = 47 \text{ mm}$. With $z_0 = 3 \text{ mm}$, we adjust the atoms location so they are only interrogated by the inline source $E_{r,1}$. To control the sam-

ple size, we vary the loading time and ramp the magnetic field gradient from 10 G/cm up to 60 G/cm before imaging. The cooling laser detuning is at -3Γ ($\Gamma = 2\pi \times 6.1 \text{ MHz}$ is the linewidth of the D2 transition). To test the spatial resolution, a 1D lattice 32Γ detuned is pulsed to write a $20 \mu\text{m}$ period atomic density grating along y . We image during and after cooling, at various Δ , τ , and probe intensities I .

Typical holograms and reconstructed images of atom samples are displayed in Fig. 3. The hologram H with a small atom sample and H_0 in the absence of the sample are nearly identical (Fig. 3A). Careful subtraction reveals the interference fringes (Fig. 3B), albeit barely visible due to the photon shot noise. We extract $E_{r,2}$ and $\varphi_{1,2} = \arg[E_{r,1} + E_{r,2}]$ from $H_0 = |E_r|^2$, by assuming a spherical wavefront for $E_{r,1}$ [22]. Our final estimation $E_r \approx \sqrt{H_0}e^{i\varphi_{1,2}}$ partly accounts for the E_{speck} effect in the E_r amplitude [26]. We also obtain the probe field $E_{r,1}(z_0) = \hat{U}_0 E_{r,1}(L)$ (Fig. 3C) [22], with E_{speck} ignored in this work [26], to simultaneously retrieve the phase shift $\phi = \text{Im}[\log(1 + E_s(z_0)/E_{r,1}(z_0))]$ and absorption coefficient $\alpha = |1 + E_s(z_0)/E_{r,1}(z_0)|^2 - 1$.

Figure 3D shows a phase shift image probed at $\Delta = 30 \Gamma$, where an $\text{SNR} \lesssim 1$ for the subtracted hologram on the camera plane (Fig. 3B) is remarkably enhanced to $\text{SNR} \approx 7$, due to the numerical focusing of $E_s(z_0)$. The resolution $\delta\phi \approx 1.7 \text{ mrad}$ is a factor of 4 smaller than the minimal noise level in phase-contrast imaging. The absorption $\alpha \approx \frac{\Gamma}{\Delta}\phi$ in Fig. 3E is below the noise floor $\delta\alpha \approx 0.4\%$ and is hardly detected. Such $\delta\phi$ and $\delta\alpha$ sensitivity levels are consistently reached under various experimental conditions (Figs. 3D-G, J, K, M, N) when the speckle noise induced blurring is below the shot noise level (Figs. 2, 4), and if N_p approaches $N_{\text{max}} = 2^{14} - 1$. The sensitivity can be further improved by reducing the intensity ratio $\kappa \approx 0.01$ with reduced z_0/L .

The atom number noise level δN_{atom} scales with $|\langle \frac{\Gamma}{2} +$

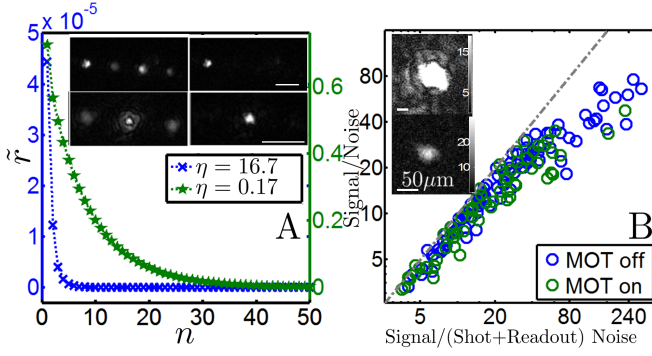


FIG. 4: A) Convergence of the twin and DC image removal algorithm for the hybrid holographic microscope with different power ratios η ($F \approx 3.8$). Inset): The one-step $|E_s^{(0)}|$ (left), and converged $|E_s^{(n=50)}|$ images for $\eta = 16.7$ (top) and $\eta = 0.17$ (bottom) (scale bar is $d = 387 \mu\text{m}$). B) SNR vs signal to the estimated (shot + camera readout) noise level for a collection of reconstructions. Inset): the converged $|E_s^{(n=50)}|$ (V/m) for a large (top) and a small (bottom) atom sample.

$i\Delta)/\frac{\Gamma}{2}$ at low probe intensities, and is minimized at $\Delta = 0$. We plot the sample column density ρ in Fig. 3K ($\Delta = 0 \Gamma$, $\tau = 800 \mu\text{s}$). The rms atom number noise level is $\delta N_{\text{atom}} = \delta \rho A_r \approx 0.8$. To see atom shot noise, we need to fix the atoms within A_r during imaging, and improve δN_{atom} further. The sample in Fig. 3L is continuously probed in the MOT with $I = 0.6 \text{ W/m}^2$ and $\tau = 10 \text{ ms}$ (with saturation intensity $I_s = 36 \text{ W/m}^2$, absorption cross-section $\sigma = 0.14 \mu\text{m}^2$ for the unpolarized atoms). Using such a weak probe, the noise level in Fig. 3L is twice the photon shot noise level due to poor subtraction of light scattered from the cooling beams.

Imaging during cooling allows us to observe the effect of light shift on the atoms by the cooling beams. For two samples of similar size, we display absorption and phase shift data for holograms taken during (Figs. 3M,N) and after (Figs. 3F,G) cooling. With $\Delta = 1.9 \Gamma$, the absorption is relatively increased when imaged while cooling, from which we infer a light shift of $\delta \approx 4 \text{ MHz}$ to the cooling transition so the dressed probe detuning $\tilde{\Delta} = \Delta - \delta$ is closer to the resonance.

We test the resolution of the microscope by imaging atoms subjected to the 1D “writing” lattice. Figures 3H,I are phase shift images of the density modulated sample with $\Delta = 1.9 \Gamma$ and $\Delta = -7.1 \Gamma$ respectively. The opposite sign of the detunings leads to advanced and retarded phase shift, as expected. The $20 \mu\text{m}$ fringe period is clearly resolved with the diffraction limited resolution.

The images reconstructed in Fig. 3 are with both twin and DC images removed. The reconstruction follows Eq. (1) and a modified form of Eq. (2) that converges slower, but stably removes the DC noise [21]. The $\tilde{r} - n$ plots in Fig. 4A characterize such a convergence. In contrast to the simulated results in Fig. 2A where $E_s(z_0)$ is known, we calculate the residual \tilde{r} defined by the difference between $E_s^{(n)}$ and $E_s^{(n=250)}$ (nearly invariant un-

der iteration.). Comparing with the simulated results in Fig. 2A, we notice that for $\eta > 1$, the hybrid geometry achieves nearly full real and twin image separation ($\tilde{r} \approx 5 \times 10^{-5}$) with a one-step reconstruction, a situation similar to the “off-axis” geometry [27], but retains the convenience of measuring forward scattering at large NA in the inline geometry. The tiny difference converges rapidly within 10 iterations. Due to the modification of Eq. (2) [21], the convergence for $\eta = 0.17$ is not as oscillatory and is twice as slow as the simulated case (Fig. 2A).

Finally, we calculate the shot noise level in H and H_0 and plot the SNR of the reconstructed $|E_s|$ vs the ratio between the signal to the estimated noise level in $|E_s|$ due to both shot noise and camera readout noise [22] (Fig. 4B). We achieve photon shot-noise limited reconstructions for samples with $\text{SNR} \lesssim 30$. Images with larger SNR in this experiment are deteriorated by the speckle noise induced blurring, similar to the simulated situation in Fig. 2B. The few data points with $\text{SNR} \lesssim 30$ that are not photon shot-noise limited are caused by changes in the speckle pattern, and relative phase fluctuation in $E_{r,1,2}$ between the recording of H and H_0 , which are not taken into account in the subtraction [22].

We have demonstrated diffraction limited holographic imaging of cold atoms with photon shot-noise limited sensitivity. The phase shift and absorption sensitivities are beyond those in standard imaging. The simplicity of the setup is in contrast to phase-contrast imaging [9], and our method can image an extended atomic sample where phase-contrast imaging is likely to be deteriorated by artifacts [28]. The technique can be integrated to atom chips [29] where nano-fabricated pinholes are back-illuminated to generate the reference fields. The method of increasing the complexity of E_r , as in the hybrid geometry, may also be useful in X-ray and electron holography [30]. As for limitations, the lengthy numerical process in this work may be sped up with advanced algorithms [31]. By including speckle noise E_{speck} in the E_r phase estimation, the SNR for a sample with large optical depth can be improved [26].

The atom number noise level $\delta N_{\text{atom}} \propto \sqrt{x_{\text{res}}^2/\sigma}$ reduces with improved imaging resolution. The moderate spatial resolution $x_{\text{res}} = 5.2 \mu\text{m}$ can be improved using a camera with a larger width w , or by magnifying the camera with lenses (Fig. 1). The aberration in the latter case is self-suppressed due to the common optical paths for E_s and E_r when $z_0 \ll L$, and can be further corrected numerically. With a factor of 10 increase of NA to 0.7 and using a camera with $Q=0.8$ ($Q=0.1$ in this work), we expect $\delta N_{\text{atom}} \approx 0.08$ with $\tau = 100 \mu\text{s}$ resonant detection. By reducing z_0 for a condensed sample, the N_{max} -limited sensitivity $\delta\phi$ can be improved further, even if the camera is magnified by lenses. With a spin-polarized sample to increase σ , $\delta N_{\text{atom}} = 0.2$ should be achievable for $\Delta = 5 \Gamma$, allowing off-resonant imaging with single atom sensitivity. This could be a scenario highly favored for precise imaging of cold atoms at high density [6].

We conclude by mentioning the possibility of non-destructive probing of multiple atoms in single sites of an optical lattice [3–5]. The idea is based on optical shielding [32]: Blue detuned light enhances the repulsion between symmetrically excited atom pairs. In the proposed scheme, atoms are trapped in single lattice sites with strong x, y confinement. A blue detuned probe and auxiliary cooling beams, all with polarization in the $x-y$ plane, switch on adiabatically so that atoms confined in single sites find new equilibrium positions separated along z . The blue-detuned molasses should allow sub-Doppler cooling of the atom array confined in the lattice site for continuous, holographic detection of the probe

light phase shift/absorption as in this work. More investigations are needed to confirm the applicability of this method, which may substantially extend the range of observables in quantum gas microscopy [3, 4].

Acknowledgments

We gratefully acknowledge early experimental contributions by M. Worsfold and B. Knight-Gregson, and helpful discussions with Dr. E. Rocco, Dr. J. V. Porto and Prof. M. Charlton.

-
- [1] M. H. Anderson, J. R. Ensher, M. R. Matthews, C. E. Wieman and E. A. Cornell, *Science* **269**, 198, 1995; K. B. Davis, M. O. Mewes, M. R. Andrews, N. J. van Druten, D. S. Durfee, D. M. Kurn and W. Ketterle, *Phys. Rev. Lett.* **75**, 3969 1995; C. C. Bradley, C. A. Sackett, J. J. Tollett, and R. G. Hulet, *Phys. Rev. Lett.* **75**, 1687, 1995.
 - [2] e. g., C. C. Bradley, C. A. Sackett, and R. G. Hulet, *Phys. Rev. A* **55**, 3951, 1997; L. E. Sadler, J. M. Higbie, S. R. Leslie, M. Vengalattore and D. M. Stamper-Kurn, *Nature* **443**, 312, 2006; N. Gemelke, X. B. Zhang, C. L. Hung and C. Chin, *Nature* **460**, 995-998, 2009.
 - [3] W. S. Bakr, J. I. Gillen, A. Peng, S. Fölling and M. A. Greiner, *Nature* **462**, 74, 2009.
 - [4] J. F. Sherson, C. Weitenberg, M. Endres, M. Cheneau, I. Bloch and S. Kuhr, *Nature* **467**, 68, 2010.
 - [5] K. D. Nelson, X. Li and D. S. Weiss, *Nature Phys.* **3**, 556, 2007.
 - [6] L. Chomaz, L. Corman, T. Yefsah, R. Desbuquois, and J. Dalibard, *New J. Phys.* **14**, 055001, 2012.
 - [7] T. Yefsah, R. Desbuquois, L. Chomaz, J. K. Günter, and J. Dalibard, *Phys. Rev. Lett.* **107**, 130401, 2011.
 - [8] Other solutions include fitting the tails of the image or to repeatedly image a fraction of the atomic sample, e. g., E. R. S. Guajardo, M. K. Tey, L. A. Sidorenkov, and R. Grimm, *Phys. Rev. A* **87**, 063601, 2013; A. Ramanathan, S. R. Muniz, K. C. Wright, R. P. Anderson, W. D. Phillips, K. Helmerson and G. K. Campbell, *Rev. Sci. Instrument* **83**, 083119, 2012.
 - [9] M. R. Andrews, D. M. Kurn, H.-J. Miesner, D. S. Durfee, C. G. Townsend, S. Inouye, and W. Ketterle, *Phys. Rev. Lett.* **79**, 553, 1997;
 - [10] J. M. Higbie, L. E. Sadler, S. Inouye, A. P. Chikkatur, S. R. Leslie, K. L. Moore, V. Savalli, and D. M. Stamper-Kurn, *Phys. Rev. Lett.* **95**, 050401 2005.
 - [11] C. Sanner, E. J. Su, A. Keshet, W. Huang, J. Gillen, R. Gommers, and W. Ketterle, *Phys. Rev. Lett.* **106**, 010402, 2011.
 - [12] R. Schley, A. Berkovitz, S. Rinott, I. Shammas, A. Blumkin, and J. Steinhauer, *Phys. Rev. Lett.* **111**, 055301, 2013.
 - [13] Shot-noise limited holography was achieved with a more complex setup in an “off-axis” geometry [27] aided by heterodyne detection. See M. Gross and M. Atlan, *Opt. Lett.*, **32**, 8, 2007. The applicability of the method for fast, high NA cold atom imaging is likely to be limited.
 - [14] D. Gabor, *Nature* **161**, 777, 1948.
 - [15] M. Kanka R. Riesenberger, P. Petruck and C. Graulig, *Opt. Lett.*, **36**, 3651, 2011.
 - [16] Lensless methods for imaging cold atoms include diffraction contrast imaging, which eliminates the twin image problem, see L. D. Turner, K. F. E. M. Domen, and R. E. Scholten in *Phys. Rev. A* **72**, 031403, 2005.
 - [17] In both standard and holographic imaging, N_{\max} can be effectively increased through pixel and frame binning.
 - [18] To be concise we may represent $E(x, y, z)$ with $E(z)$.
 - [19] *Introduction to Fourier Optics Third Edition*, J. W. Goodman (Roberts and Company, 2005).
 - [20] G. Koren, D. Joyeux and F. Polack, *Opt. Lett.* **16**, 1979, 1991.
 - [21] Equation (2) assumes $|E_s|^2 \ll |E_r|^2$ everywhere on the camera. When this is not valid, Eq. (2) is modified to remove the DC term in Eq. (1). See [22].
 - [22] See auxiliary material.
 - [23] J. J. Hope and J. D. Close, *Phys. Rev. Lett.* **93**, 180402, 2004; *Phys. Rev. A* **71**, 043822, 2005.
 - [24] A similar comparison was made by S. Kadlecek et al in *Opt. Lett.* **26**, 137, 2001 where a spatial heterodyne method retrieves E_s with limited NA.
 - [25] *Laser Cooling and Trapping*, H. Metcalf and P. van der Straten (Springer-Verlag, 1999).
 - [26] To include E_{speck} in the estimation of φ , one can locate the distant point-like scatterers holographically. We have developed an algorithm for such inclusion that shows suppression of the speckle-induced blurring as in Figs. 2B, 4B. The results will be published elsewhere.
 - [27] E. N. Leith and J. Upatnieks. *J. Opt. Soc. Am.* **54**, 1295, 1964.
 - [28] A. H. Bennett, H. Osterberg, H. Jupnik, and O. W. Richards, *Phase microscopy; principles and applications* (Wiley & Sons, New York USA, 1951).
 - [29] J. Fortagh and C. Zimmermann, *Science* **307**, 860, 2005.
 - [30] For example, H. Jiang et al, *Phys. Rev. Lett.* **110**, 205501, 2013; M. Germann, T. Latychevskaia, C. Escher, and H. Fink, *Phys. Rev. Lett.* **104**, 095501, 2010.
 - [31] S. R. Segal, Q. Diot, E. A. Cornell, A. A. Zozulya, and D. Z. Anderson, *Phys. Rev. A* **81**, 053601, 2010.
 - [32] K. Suominen, M. Holland, K. Burnett and P. Julienne, *Phys. Rev. A* **51**, 1446, 1995; V. A. Yurovsky and A. Ben-Reuven, *Phys. Rev. A* **55**, 3772, 1997.

Auxiliary Material

I. *Extracting the reference field.* To extract the reference field E_r , we only need to estimate $\varphi = \arg[E_r]$ so that $E_r = \sqrt{H_0}e^{i\varphi}$. With large L and tightly focused $E_{r,j}$ ($j = 1, 2$), we assume the wavefronts $E_{r,j}(\mathbf{R}) \propto \sqrt{H_j}e^{ik|\mathbf{R}-\mathbf{r}_j|}$ with $\mathbf{R} = (x, y, L)$ on the camera plane to be well-approximated by spherical waves from the focal points \mathbf{r}_j ($j = 1, 2$). Here H_1 and H_2 are intensity images taken individually when the inline $E_{r,1}$ or off-axis $E_{r,2}$ is on respectively. In the following we describe the procedure to determine the location of the focal points \mathbf{r}_1 and \mathbf{r}_2 , and additional adjustments to estimate $E_r(L)$ for image reconstruction, as well as to estimate $E_r(z_0)$ for phase shift ϕ and absorption coefficient α retrieval.

We decide the origin $x = y = 0$ on the camera plane by considering the projection of \mathbf{r}_1 onto the camera. For this we adjust the $H_1 = |E_{r,1}|^2$ intensity pattern recorded on the camera so that it is centered and appears as a symmetric Gaussian profile. We then fit H_1 with a 2D Gaussian $H_{1,f}$ and set the center of the fit as $x = y = 0$. With an estimate of the \mathbf{r}_1 source-camera separation L , the location \mathbf{r}_2 is retrieved by numerically propagating the hologram H_0 with $E = H_0/E_{r,1}^*$ to its focal plane (with knowledge of the $\mathbf{r}_{1,2}$ relative position, the twin image at $-\mathbf{r}_2$ is easily identified). The relative displacement $|\mathbf{r}_2 - \mathbf{r}_1| = d = 387.0 \mu\text{m}$, measured before the installation, is used to calibrate the L parameter in $E_{r,1}$.

The holographic reconstruction of the $E_{r,2}$ focal point not only allows us to decide L and \mathbf{r}_2 , but also provides an estimate of the relative phase ϕ_r between $E_{r,2}$ and $E_{r,1}$. We therefore reach an estimate $E_r^{(0)}(a_1, a_2, \phi) = a_1\sqrt{H_{1,f}}e^{ik|\mathbf{R}-\mathbf{r}_1|} + a_2\sqrt{H_{2,f}}e^{ik|\mathbf{R}-\mathbf{r}_2|+i\phi_r}$ on the camera plane with $a_1 = a_2 = 1$ ($H_{2,f}$ is a 2D fit of the H_2 intensity pattern.). To improve the accuracy of the estimation, we numerically minimize the difference $H_0 - |E_r^{(0)}(a_1, a_2, \phi_r)|^2$ to achieve the optimal $E_{r,\text{opt}}^{(0)} = a_{1,\text{opt}}\sqrt{H_{1,f}}e^{ik|\mathbf{R}-\mathbf{r}_1|} + a_{2,\text{opt}}\sqrt{H_{2,f}}e^{ik|\mathbf{R}-\mathbf{r}_2|+i\phi_{r,\text{opt}}}$. Finally, we use $\varphi_{1,2} = \arg[E_{r,\text{opt}}^{(0)}]$ to approximate $\varphi = \arg[E_r]$ in this work so that $E_r(L) \approx \sqrt{H_0}e^{i\varphi_{1,2}}$.

From the estimated $E_r(L)$ it is straightforward to calculate $E_r(z_0) = \hat{U}_0 E_r(L)$. The result, however, is contaminated by the boundary artifacts during fast Fourier transforms. To avoid the artifacts we expand the fitted $H_{1,f}$ and $H_{2,f}$ onto a grid twice as large as the camera, so that both fitted intensity patterns are well-contained within the grid. Similar to the $E_r(L)$ estimation, the approximation $E_r(z_0) \approx \hat{U}_0 E_{r,\text{opt}}^{(0)}$ ignores speckle noise.

II. *Iterative twin and DC removal.* The algorithm in Eq. (2) assumes a negligible DC term in Eq. (1) (i.e. $|E_s|^2 \ll |E_r|^2$ everywhere on the camera). To remove the DC term the iterative twin image removal algorithm in Eq. (2) is modified. Using our estimation of E_s at each iteration $E_s^{(n)}$, we calculate the corresponding DC term $\approx |\hat{U}_0^{-1} \hat{P} E_s^{(n)}|^2$ and then subtract it away from the hologram $H - H_0$ and thus $E_H = (H - H_0)/E_r^*$. The

algorithm in Eq. (2) is modified to

$$\begin{aligned} E_s^{(0)} &= \hat{U}_0 E_H, \\ \tilde{E}_s^{(0,n)} &= \hat{U}_0 \left(E_H - |\hat{U}_0^{-1} \hat{P} E_s^{(n)}|^2 / E_r^* \right), \\ E_s^{(n+1)} &= (1 - \nu) \hat{P} E_s^{(n)} + \nu \hat{U}_0 \hat{C} \hat{U}_0^{-1} \left(\tilde{E}_s^{(0,n)} - \hat{P} E_s^{(n)} \right). \end{aligned} \quad (\text{A.1})$$

In Eq. (A.1) a parameter ν is introduced to control the convergence speed. In the original algorithm (Eq. (2)) $\nu = 1$. Due to the additional step to remove the DC term, the iterative algorithm becomes nonlinear, and we find it can be unstable when E_s is large. Adjusting the parameter ν can improve the stability and we set $\nu = 0.5$ in this work. The convergence speed is correspondingly a factor of two slower (Fig. 4A), while in addition the oscillatory feature (Fig. 2A) in the convergence is suppressed.

III. *Optimal background subtraction.* Practically, the holograms H and H_0 , and the intensity patterns H_1 and H_2 , are affected by power and phase fluctuations of the laser, as well as background ambient light. For retrieving E_r using H_0 , H_1 and H_2 as in section I., we simply take a background image B_0 with the same exposure time as H_0 and subtract it away directly. The subtraction $H - H_0$ in Eq. (1), however, requires a higher precision. We have developed a two-step optimization procedure for the subtraction as following, both using a Matlab optimization program “fminsearch”.

First, by taking advantage of the characteristic two point interference on the camera, we optimize the subtraction $H_R^{(0)}(b) = H - bH_0$, with parameter b to account for an overall power fluctuation of the laser between the two recordings. The optimization starts with the complex field $E(b) = H_R^{(0)}(b)/E_{r,1}^*$ to be propagated to $z = 0$, $\hat{U}(-L)E(b)$, where three spot images are formed. We isolate the spot corresponding to the off-axis source at $\mathbf{r}_2 = (d, 0, 0)$ and calculate its residual power $dP(b)$ (The other two spots correspond to the inline source and the twin image of the off-axis source.). These steps are repeated until $dP(b)$ is minimized at an optimal choice $b = b_{\text{opt}}$. To ensure that the presence of the atomic sample in H does not affect our choice of b_{opt} , we apply a mask that blocks the data in both H and H_0 where we expect the geometric shadow of the sample, before the optimization starts.

Such optimization for $b = b_{\text{opt}}$ based on the interference fringes cannot account for any relative power fluctuation between $E_{r,1}$ and $E_{r,2}$. In addition, any fluorescence from the atoms would cause a uniform background f_{bk} . We account for these effects, together with the background ambient light, using a four parameter optimization process with parameters c_j , $j = 1, 2, 3, 4$.

$$H_R = H - b_{\text{opt}} H_0 - c_1 B + c_2 B_0 - c_3 f_{\text{bk}} - c_4 P_f. \quad (\text{A.2})$$

Here $P_f = H_{f,1} - H_{f,2}$ accounts for power fluctuation between $E_{r,1}$ and $E_{r,2}$, $f_{\text{bk}} = 1$ and B is the ambient background image with the same exposure time as H .

The complex field $E(c_j) = H_R(c_j)/E_r^*$, ($j = 1, 2, 3, 4$) is then propagated via \hat{U}_0 to $z = z_0$ where we expect the in-focus atom image $E_s(z_0)$ as well as the out-of-focus twin and DC images (as in Fig. 1). We use the mask $1 - \hat{P}$ to exclude E_s . The leftover atom twin images are converted into a single real image and refocused to $z = z_0$ using the $\hat{U}_0 \hat{C} \hat{U}_0^{-1}$ operation as in Eq. (2), before it is also excluded via $1 - \hat{P}$. The two-step exclusions ensure that the final image is nearly free of atomic signal, from which we calculate the rms noise level $N(c_j)$ to be minimized at $c_{j,\text{opt}}$ and thus the final $H_{R,\text{opt}}$ which is considered as the “ $H - H_0$ ” to obtain E_H in Eq. (1). This is the most time-consuming part of our reconstruction process, and takes approximately 10 mins with a PC (Intel Core i5-2400 CPU, 3.1 GHz).

IV. Propagation of shot noise. The rms shot noise level in the holograms, being proportional to the pixel count $N_p = \sqrt{H A_p Q \tau / \hbar \omega}$, is given by $n_H = H / \sqrt{H A_p Q \tau / \hbar \omega}$ and similarly $n_{H_0} = H_0 / \sqrt{H_0 A_p Q \tau / \hbar \omega}$. The associated shot noise δE_H of the complex field E_H in Eq. (1), defined at each pixel with area A_p , has a rms level of:

$$n_{EH} = |\sqrt{n_H^2 + n_{H_0}^2} / E_r^*|, \quad (\text{A.3})$$

$$= \sqrt{2 \hbar \omega / A_p Q \tau}.$$

Here we assume $n_H = n_{H_0}$. To derive the rms level of the shot noise field δE_a at the atoms location ($z = z_0$), we simply evaluate the intensity contribution $|\hat{U}_0 \delta E_H|^2$ from each camera pixel on which δE_H has a random but uniform amplitude. The contribution is then summed over all the pixels to give the intensity of δE_a .

More specifically, we consider the field δE_H through each pixel of the camera, with wavefront area restricted by the tiny pixel area A_p , as part of spherical waves propagating toward the focal points \mathbf{r}_1 and \mathbf{r}_2 . It is thus straightforward to calculate the noise level δE_0 near the point sources, $\mathbf{r} = O(d)$, via Kirchhoff's diffraction theorem and further a 2D integration of the intensity contribution over all the pixels. The final result is:

$$n_{E,\mathbf{r}=O(d)} = \sqrt{2 \hbar \omega / \tilde{A}_r Q \tau}, \quad (\text{A.4})$$

$$\tilde{A}_r = \lambda^2 / (4 \text{NA} \times \tan^{-1}(\text{NA})).$$

Here $\text{NA} = w / \sqrt{w^2 + 4L^2}$ is the numerical aperture of the point sources spanned by the camera. With $z_0 \ll L$ the noise level near the atom location $n_{E,a} \approx n_{E,\mathbf{r}=O(d)}$. With $\tilde{A}_r \approx A_r$, we reach an estimate of the rms level of shot noise δE_a near the atom location:

$$n_{E,a} \approx \sqrt{2 \hbar \omega / A_r Q \tau} \quad (\text{A.5})$$

V. The final shot noise level after iteration The inclusion of shot noise modifies the input of the iteration in Eq. (2) as $\tilde{E}_s^{(0)} = E_s^{(0)} + \delta E_a$, while the complex field E_H is modified as $\tilde{E}_H = E_H + \delta E_H$. As the iteration series

converges to $\tilde{E}_s = E_s(z_0) + \delta E_s$, instead of $\delta E_s \rightarrow 0$ in the noiseless case, it is easy to show that the following relation holds (here for simplicity we consider $|E_s|^2 \ll |E_r|^2$ as in Eq. (2) so that the DC term can be ignored):

$$\delta E_s = \delta E_a - \hat{U}_0 \hat{C} \hat{U}_0^{-1} \hat{P} \delta E_s. \quad (\text{A.6})$$

The final noise δE_s , as a functional of the shot noise δE_a specified by Eq. (A.4), is difficult to calculate analytically. However, if $\hat{P} \delta E_s$ is, as verified numerically, a uniform shot noise pattern filtered by the aperture \hat{P} , while further, the twin image term $\hat{U}_0 \hat{C} \hat{U}_0^{-1} \hat{P} \delta E_s$ is not correlated with the shot noise δE_a in Eq. (A.6), then the intensities of the two terms on the right add up:

$$n_{E_s}^2 = n_{E,a}^2 + \xi^2 n_{E_s}^2. \quad (\text{A.7})$$

Here ξ is the ratio of the rms level between $\hat{U}_0 \hat{C} \hat{U}_0^{-1} \hat{P} \delta E_s$ and δE_s . The final result of the shot noise level becomes:

$$n_{E_s} \approx \frac{\sqrt{2 \hbar \omega / A_r Q \tau}}{\sqrt{1 - \xi^2}}. \quad (\text{A.8})$$

For the traditional inline geometry $\xi_{\text{inline}} = 1 / (1 + \frac{2w/L}{a/z_0})$ ($z_0 \ll L$), which can be derived by considering the area ratio of the apertured shot noise given by \hat{P} and its NA-limited shadow at the twin image plane. For the hybrid geometry $\xi \approx (1 - \eta) \xi_{\text{inline}}$ for $\eta < 1$. In this work $\xi \approx 0.1$, so the increase of the shot noise level from $n_{E,a}$ to n_{E_s} due to the twin-image removal is less than 1%.

VI. Shot-noise limited SNR, and N_{max} -limited sensitivity With the noise level of δE_s specified by Eq. (A.8), the $\text{SNR} = \sqrt{\langle |E_s(z_0) / n_{E_s}|^2 \rangle}$ over a particular resolution area A_r , is given by $\text{SNR} = \sqrt{N_s / 2}$ with $N_s = \langle |E_s(z_0)|^2 \rangle A_r Q \tau / \hbar \omega$ as in the main text (we consider $\xi^2 / 2 \ll 1$).

On the other hand, for a camera with a maximum count N_{max} , the relation $|E_r(L)|^2 A_p Q \tau / \hbar \omega < N_{\text{max}}$ needs to be obeyed for most of pixels on the camera. Thus by considering the $\text{SNR} = 1$ limit, the minimum detectable E_s must obey $\left| \frac{E_s(z_0)}{E_r(L)} \right| > \sqrt{\frac{2 A_p}{N_{\text{max}} A_r}}$, or,

$$\left| \frac{E_s(z_0)}{E_r(z_0)} \right| > \sqrt{\frac{2 \kappa A_p}{N_{\text{max}} A_r}}, \quad (\text{A.9})$$

with $\kappa = |E_r(L)|^2 / |E_r(z_0)|^2$. Equation (A.9) also provides the minimum detectable phase shift $\delta \phi$, as well as half of the minimum detectable absorption coefficient $\delta \alpha$.

VII. SNR and shot noise level in the image data To obtain the SNR for the experimental images, we define the signal as the mean value of the reconstructed $|E_s|$ above 60% of its maximum. The noise level is given by $\sqrt{\langle |E_s|^2 \rangle_D}$, where D is the area of an annulus surrounding \hat{P} with ring width equal to a .

The shot noise level in the reconstruction is simply estimated via the formula $n_H = H / \sqrt{H A_p Q \tau / \hbar \omega}$ and $n_{H_0} = H_0 / \sqrt{H_0 A_p Q \tau / \hbar \omega}$ for the holograms H ,

H_0 respectively and then follows Eq. (A.3) to obtain n_{EH} . A ratio $\sqrt{A_p/A_r}$ is then multiplied according to Eqs. (A.3)(A.5) to obtain the level $n_{Ea} \approx n_{Es}$ according to Eq. (A.8). The camera readout noise at 8 counts/pixel for both H and H_0 is added to the photon shot noise quadratically. We also include the shot noise in the ambient background B and B_0 , which are averaged over 9 images and contribute negligibly to the overall noise level.

VIII. *Sub-pixel resolution, field and depth of view.*

To achieve sub-pixel resolution, we simply split each pixel in the camera-recorded hologram into M^2 new pixels, each with new pixel size $\tilde{x}_{\text{cam}} = x_{\text{cam}}/M \leq x_{\text{res}}$.

An important advantage of the holographic microscope is its ability to reconstruct the image of an object within its volume of view, given by the ability of the camera to record the interference fringes determined by the Whittaker-Shannon sampling theorem [19], thereby enabling a 3D volumetric view of sparse objects.